Loss of SMPD4 Causes a Developmental Disorder Characterized by Microcephaly and Congenital Arthrogryposis

Pamela Magini,[1,40] Daphne J. Smits,[2,40] Laura Vandervore,[2,3] Rachel Schot,[2] Marta Columbaro,[4] Esmee Kasteleijn,[2] Mees van der Ent,[5] Flavia Palombo,[6] Maarten H. Lequin,[7] Marjolein Dremmen,[8] Marie Claire Y. de Wit,[9] Mariasavina Severino,[10] Maria Teresa Divizia,[11] Pasquale Striano,[12,13] Natalia Ordonez-Herrera,[14] Amal Alhashem,[15,16] Ahmed Al Fares,[15,16] Malak Al Ghamdi,[17] Arndt Rolfs,[14] Peter Bauer,[14] Jeroen Demmers,[18] Frans W. Verheijen,[2] Martina Wilke,[2] Marjon van Slegtenhorst,[2] Peter J. van der Spek,[19] Marco Seri,[20] Anna C. Jansen,[3,21] Rolf W. Stottmann,[22] Robert B. Hufnagel,[23] Robert J. Hopkin,[22,24] Deema Aljeaid,[25] Wojciech Wiszniewski,[26,27] Pawel Gawlinski,[27] Milena Laure-Kamionowska,[28] Fowzan S. Alkuraya,[29] Hanah Akleh,[30] Valentina Stanley,[31] Damir Musaev,[31] Joseph G. Gleeson,[31] Maha S. Zaki,[32] Nicola Brunetti-Pierri,[33,34] Gerarda Cappuccio,[33,34] Bella Davidov,[35] Lina Basel-Salmon,[35,36,37] Lily Bazak,[35] Noa Ruhrman Shahar,[35] Aida Bertoli-Avella,[14] Ghayda M. Mirzaa,[38,39] William B. Dobyns,[38] Tommaso Pippucci,[1,*] Maarten Fornerod,[5,41] and Grazia M.S. Mancini[2,41,*]

Sphingomyelinases generate ceramide from sphingomyelin as a second messenger in intracellular signaling pathways involved in cell proliferation, differentiation, or apoptosis. Children from 12 unrelated families presented with microcephaly, simplified gyral pattern of the cortex, hypomyelination, cerebellar hypoplasia, congenital arthrogryposis, and early fetal/postnatal demise. Genomic analysis revealed bi-allelic loss-of-function variants in *SMPD4*, coding for the neutral sphingomyelinase-3 (nSMase-3/SMPD4). Overexpression of human Myc-tagged SMPD4 showed localization both to the outer nuclear envelope and the ER and additionally revealed interactions with several nuclear pore complex proteins by proteomics analysis. Fibroblasts from affected individuals showed ER cisternae abnormalities, suspected for increased autophagy, and were more susceptible to apoptosis under stress conditions, while treatment with *siSMPD4* caused delayed cell cycle progression. Our data show that SMPD4 links homeostasis of membrane sphingolipids to cell fate by regulating the cross-talk between the ER and the outer nuclear envelope, while its loss reveals a pathogenic mechanism in microcephaly.

[1]Medical Genetics Unit, S.Orsola-Malpighi Hospital, via Massarenti 9, 40138 Bologna, Italy; [2]Department of Clinical Genetics, ErasmusMC University Medical Center Rotterdam, Dr. Molewaterplein 40, 3015 GD Rotterdam, the Netherlands; [3]Vrije Universiteit Brussel, Centrum Medische Genetica, Laarbeeklaan 101, 1090 Brussels, Belgium; [4]Laboratory of Musculoskeletal Cell Biology, IRCCS Istituto Ortopedico Rizzoli, 40136 Bologna, Italy; [5]Department of Cell Biology, ErasmusMC University Medical Center Rotterdam, Dr. Molewaterplein 40, 3015 GD Rotterdam, the Netherlands; [6]IRCCS Institute of Neurological Sciences of Bologna, Bellaria Hospital, 40139 Bologna, Italy; [7]Department of Radiology, University medical center Utrecht, Heidelberglaan 100, 3584 CX Utrecht, the Netherlands; [8]Department of Radiology, Sophia Children's hospital, ErasmusMC University Medical Center Rotterdam, Dr. Molewaterplein 40, 3015 GD Rotterdam, the Netherlands; [9]Department of Child Neurology, Sophia Children's hospital, ErasmusMC University Medical Center Rotterdam, Dr. Molewaterplein 40, 3015 GD Rotterdam, the Netherlands; [10]Neuroradiology Unit, IRCCS Istituto Giannina Gaslini, 16147 Genova, Italy; [11]UOC Genetica Medica, IRCCS Istituto Giannina Gaslini, 16147 Genova, Italy; [12]Pediatric Neurology and Muscular diseases Unit, IRCCS Istituto Giannina Gaslini, 16147 Genova, Italy; [13]Department of neursciences, Rehabilitation, Ophthalmology, Genetics, Maternal and Child Health, University of Genova, 16126 Genova, Italy; [14]CENTOGENE AG. Am Strande 7, 18055 Rostock, Germany; [15]Department of Pediatrics, Prince Sultan Military Medical City, Riyadh 12233, Saudi Arabia; [16]Department of Pediatrics, College of Medicine, Qassim University, Qassim 52571, Saudi Arabia; [17]Department of Pediatrics, College of Medicine, King Saud University, Riyadh 11451, Saudi Arabia; [18]Proteomics Center, Room Ee-679A, Erasmus University Medical Center. Wytemaweg 80, 3015 CN Rotterdam, the Netherlands; [19]Department of Pathology, Clinical Bioinformatics, ErasmusMC University Medical Center PO Box, 3000CA Rotterdam, the Netherlands; [20]Medical Genetics Unit, Department of Medical and Surgical Sciences, University of Bologna, via Massarenti 9, 40138 Bologna, Italy; [21]Pediatric Neurology Unit, UZ Univeristy of Brussel, Laarbeeklaan 101, 1090 Brussels, Belgium; [22]Department of Human Genetics, Division of Developmental Biology Cincinnati Children's Hospital Medical Center, 3333 Burnet Avenue, MLC 7016, Cincinnati, OH 45229, USA; [23]Medical Genetics and Ophthalmic Genomics Unit, National Eye Institute, National Institutes of Health, 10 Center Drive, Building 10, Room 10N109, Bethesda, MD 20892, USA; [24]Department of Pediatrics, University of Cincinnati, College of Medicine, 3333 Burnet Ave., ML 4006, Cincinnati, OH 45229, USA; [25]Department of Human Genetics, Faculty of Medicine, King Abdulaziz University, Jeddah 21589, Saudi Arabia; [26]Oregon Health & Sciences University, 3181 SW Sam Jackson Park Road L103, Portland, OR, USA; [27]Institute of Mother and Child, Kasprzaka 17a, 02-211 Warsaw, Poland; [28]Department of Experimental and Clinical Neuropathology, Mossakowski Medical Research Centre Polish Academy of Sciences, Pawinskiego 5, 02-106 Warsaw, Poland; [29]Department of Genetics, King Faisal Specialist Hospital and Research Center, Riyadh, Saudi Arabia; [30]Department of Obstetrics and Gynecology, King Faisal Specialist Hospital and Research Center, Riyadh 12713, Saudi Arabia; [31]Laboratory for Pediatric Brain Disease, Department of Neurosciences, Howard Hughes Medical Institute, University of California, San Diego, San Diego, CA 92093, USA; [32]Human Genetics and Genome Research Division, Clinical Genetics Department, National Research Centre, Cairo 12622, Egypt; [33]Department of Translational Medicine, University of Naples "Federico II," Naples 80131, Italy; [34]Telethon Institute of Genetics and Medicine (TIGEM), Pozzuoli 80078, Italy; [35]Department of Medical Genetics, Recanati Genetic Institute Rabin Medical Center, Beilinson Campus, Petah Tikva, 49100 Tel Aviv, Israel; [36]Felsenstein Medical Research Center, Rabin Medical Center, Petah Tikva 49100, Israel; [37]Sackler Faculty of Medicine, Tel Aviv University, Tel Aviv 69978, Israel; [38]Department of Pediatrics, University of Washington, Seattle, WA 98195, USA; [39]Center for Integrative Brain Research, Seattle Children's Research Institute, Seattle, WA 98101, USA
[40]These authors contributed equally to this work
[41]These authors contributed equally to this work
*Correspondence: tommaso.pippucci@gmail.com (T.P.), g.mancini@erasmusmc.nl (G.M.S.M.)
https://doi.org/10.1016/j.ajhg.2019.08.006.

Introduction

Sphingolipids constitute a class of lipids with essential cellular functions, including the modulation of physical properties of cell membranes and regulation of transmembrane and peripheral membrane proteins. In addition, sphingolipids regulate the production of biosynthetic intermediates with roles as signaling molecules, such as sphingosine and ceramides.[1] Sphingolipids are highly enriched in the nervous system and are important for proper brain development and function.[2]

Sphingomyelin is the most abundant eukaryotic sphingolipid and regulation of its metabolism is critical for cell function. Dysfunction of enzymes regulating the balance between sphingomyelin synthesis and degradation have been reported in many pathologies affecting the central nervous system.[3] Sphingomyelinases hydrolyze sphingomyelin into ceramide and phosphorylcholine. To date, one acid sphingomyelinase (SMPD1) and four neutral sphinogmyelinases (nSMases) have been characterized in mammals: nSMase1 (SMPD2), nSMase2 (SMPD3), nSMase3 (SMPD4), and a mitochondria-associated MA-nSMase (SMPD5), respectively encoded by *SMPD1* (MIM: 607608), *SMPD2* (MIM: 603498), *SMPD3* (MIM: 605777), *SMPD4* (MIM: 610457), and *SMPD5*. Although nSMase-3 (from now on indicated as SMPD4), encoded by *SMPD4*, has no significant sequence homology with other sphingomyelinases, some papers reported its catalytic activity and described regulation of its expression by tumor necrosis factor and p53, implicating this protein in response to cellular stress.[4–6] SMPD4 is a 866 amino acid long protein with a protein-protein interaction domain and a C-terminal transmembrane domain close to the putative enzyme active site, which includes a potential N-glycosylation site.[5,6] Subcellular localization experiments have shown the presence of SMPD4 at the endoplasmic reticulum (ER) and the Golgi apparatus. In independent studies, proteomics analysis of nuclear fractions detected SMPD4 at the nuclear envelope.[4,5,7,8] In this latter context, SMPD4 was identified as nuclear envelope transmembrane protein-13, NET13.

Defects in genes encoding proteins of this sphingomyelinase family are known to cause developmental disorders linked to intracellular organelle dysfunction. Inactivation of *Smpd3*, the murine homolog of human *SMPD3*, impairs Golgi vesicular transport, perturbs protein homeostasis, and induces ER stress, leading to apoptosis, growth inhibition, and development retardation in mice.[9] To date, human variants have only been reported in *SMPD1*, causing lysosomal storage disorders Niemann-Pick disease type A and B (MIM: 607608).

Here, we report on 12 families including individuals presenting with congenital microcephaly with simplified gyral pattern, mild cerebellar hypoplasia, severe encephalopathy, congenital arthrogryposis, diabetes mellitus, cardiomyopathy, and early demise. 23 affected individuals were available for sequencing, all of whom harbor bi-allelic variants in *SMPD4*. We provide clinical and neuroimaging data of this cohort to describe the disease phenotype, together with functional evidence for a role of SMPD4 in cell fate and mitosis.

Material and Methods

Cohort Recruitment

Clinical data and material from affected individuals, belonging to 12 unrelated families, were recruited through collaboration within the European Network on Brain Malformations (Neuro-MIG, COST Action CA16118). Six families were recruited through collaborative sharing of genomic variants through Genematcher.[10] The study was approved by the local IRBs (Erasmus MC University Medical Center Rotterdam, protocol METC-2012387). Written informed consent was obtained from all parents/caretakers by each physician. Fibroblasts from affected individuals used in this study were obtained from skin biopsies previously sampled for routine diagnostic testing.

Pathology

Complete neuropathological assesment of the brain (family 7, II-2) was performed according to standard procedures. For microscopic evaluation, fresh-frozen paraffin-embedded sections of the brain tissue were stained with hematoxylin-eosin and cresyl violet.

Genomic Microarrays and Homozygosity Mapping

Blood-derived DNA samples from individuals V-1, V-2, V-3, and VI-1 of family 1 were hybridized to the arrays according to the Affymetrix standard protocol for the GeneChip Mapping 250K NspI Array. Genotype data analysis was performed with Affymetrix GeneChip Genotyping analysis software (GTYPE) using the BRLMM algorithm. The obtained .CEL and .CHP files were used for homozygosity mapping in CNAG version 3.0.

Exome Sequencing

Exome sequencing was performed on DNA isolated from blood or cultured skin fibroblasts derived from probands and family members in ten different laboratories. WES/WGS data are deposited internally at the Erasmus MC and in each medical institute referring the individuals with *SMPD4* variants, in respect to the privacy of the families. Details of sequencing and analysis pipelines are described in the Supplemental Methods.

Fibroblast Culture

Fibroblasts from skin biopsies of affected individuals V-3 and VI-1 from family 1 and individual V-2 of family 2 and four sex- and age-matched healthy individuals were grown in Dulbecco Modified Eagle Medium supplemented with 10% fetal bovine serum (FBS), 1% L-glutamine (v/v), and 1% penicillin/streptomycin (v/v) (DMEM with serum) at 37°C and 5% CO_2. Cells were enzymatically detached from T75 confluent flasks by using 1 mL trypsin/EDTA (0.25%).

RNA Sequencing

Skin fibroblasts from individuals V-3 and VI-1 from family 1 and four different healthy age-matched control subjects were cultured to 80% confluence in T175 flasks, before lysis with TRIzol Reagent (Invitrogen, 15596026) and RNA isolation with RNeasy mini kit

(QIAGEN, 74106). Strand-specific mRNA-seq libraries for the Illumina platform were generated with a poly-A selection and sequenced at GenomeScan. Fastq files from forward and reverse reads were aligned to reference genome hg38 with the STAR aligner tool (v.2.4.2a) and quantified per gene with HTSeq using hg38 exon coordinates (release 86). Count data were used for differential gene expression using the edgeR package in R.

RT-qPCR

Total RNA was extracted from cultured skin fibroblasts using RNeasy mini columns (QIAGEN) according to the manufacturer's protocol. 1 μg of RNA was reverse transcribed in a total reaction volume of 20 μL with the iScript cDNA synthesis kit (Bio-Rad Laboratories) according to manufacturer's protocol. Real-time qPCR was performed using iTaq Universal SYBR Green Supermix (BioRad). Primers for RT-qPCR analysis are shown in Table S1.

Electronic Microscopy on Fibroblast Culture

Fibroblast pellets from age- and gender-matched healthy or affected individuals, at passages number between 3 and 12, were fixed with 2.5% glutaraldehyde 0.1 M cacodylate buffer (pH 7.6) for 1 h at room temperature. After post-fixation with 1% osmium tetroxide in cacodylate buffer for 1 h at 4°C, pellets were dehydrated in an ethanol series and embedded in Epon resin. Ultrathin sections stained with uranyl-acetate and lead citrate were observed with a Jeol Jem-1011 transmission electron microscope.

SMPD4 Knockdown and Flow Cytometry

Healthy volunteers' fibroblasts were plated in a concentration of 1.5×10^4 cells/cm^2 on 24 mm coverslips cultured in 2 mL DMEM with serum in a 6-well plate. The next day, cell confluency reached 80% and culture media was replaced with 2 mL DMEM without serum (Lonza). 1 μL SMPD4 siGenome siRNA (20 μM) Dharmacon smartpool (M-020681-02-0005) and 2 μL DharmaFECT 3 Transfection Reagent (Dharmacon) were incubated for 5 min at room temperature with 67 μL DMEM without serum. Lipofectans and smartpool were added together for 20 min at room temperature, prior to transfection. The mixture was added to each well in a dropwise manner. After 3 h, 10% FCS was supplemented to the wells and cells were fixated after 24 h *SMPD4* knockdown with methanol for 10 min at −20°C.

Flow cytometry was performed on all fibroblasts cell lines and siRNA-treated fibroblasts. 1×10^6 fibroblast cells were pelleted and fixed with 4% Paraformaldehyde for 30 min on ice. After washing with 1 × PBS/10%FCS, cells were permeabilized with 0.1% Triton X-100 for 10 min on ice. DNA was stained with 1 μg/mL Hoechst 33342 and cells were counted on BD LSRFortessa Cell Analyzer with 20 000 events counted per cell line. Cell cycle analysis was performed in FlowJo v.7.6.5.

Plasmid Constructs

Wild-type human *SMPD4* (GenBank: NM_017951) Myc-DDK-tagged ORF Clone was purchased from Origene (CAT#: RC219824). 50 μL semi-competent homemade *Escherichia coli* XL10-Gold Bacteria strains were thawed on ice for 20 min and subsequently incubated for 15 min with 1 μg wild-type SMPD4 plasmid. Transformation of the bacterial cells was induced through a heat shock at 42°C for 2 min. 800 μL Luria-Bertani (LB) broth (EZ Mix, Lennox) was added to the cells and placed under agitation (200 rpm, 40 min, 37°C). Selection of transformed cells was performed overnight on LB-Ampicillin agar plates at 37°C. Vector-positive colonies were grown to 50 mL midiprep. Plasmid DNA was isolated with the QIAGEN Plasmid Plus Midi kit. pcDNA3.1/myc-His(-)/lacZ (Thermo Fisher Scientific) was used as a negative control and kindly donated by Dr. Mark Nellist. The full length and sequence of *SMPD4* cDNA in the plasmid was confirmed by capillary sequencing prior to performing the transfections.

Exogenous SMPD4 Expression in HEK293T Cells

Human Embryonic Kidney HEK293T cells were plated at 5×10^4 cells/cm^2 on 24 mm coverslips (Thermo Fisher Scientific) cultured in 2 mL DMEM with serum in a 6-well plate or 10 cm Petri dishes for immunoprecipitation. The following day, culture media was replaced with 2 mL DMEM without serum. Per 10 cm^2, 15 μg SMPD4 plasmid was added to 625 μL DMEM without serum at room temperature and 45 μL/10 cm^2 Lipofectamine 2000 Transfection Reagent (Thermo Fisher Scientific) was added to 625 μL DMEM without serum. These tubes were mixed and incubated 5 min at room temperature prior to transfection. The appropriate volume was added to each dish in a dropwise manner. After 3 h, 10% FCS and 1% PenStrep was supplemented to the dishes. After 24 h transfection, cells were fixated with methanol for 10 min at −20°C or lysed for western blot and immunoprecipitation.

Interactome Analysis

Immunoprecipitation of exogenous Myc-tagged SMPD4 was performed after transfection in HEK293T cells. 30 μL of EZview Red Anti-c-Myc affinity gel beads (Sigma Aldrich) were washed with TNE-1% lysis buffer. Transfected HEK293 cells were washed with 1× dPBS on ice and lysed with 800 μL TNE-1% lysis buffer. Lysates were incubated on ice for 10 min and centrifuged at 10,000 × *g* for 10 min at 4°C. The supernatant was added to the washed Myc affinity gel beads and incubated overnight at 4°C. The following day, mixtures were washed 3 times with TNE-1% lysis buffer and centrifuged at 1,000 × *g* for 15 s at 4°C. The bead-pellets were transferred to Pierce spin columns. The beads were thoroughly washed in 50 mM ammonium bicarbonate, followed by a reduction in 50 mM Tris/HCl (pH 8.2) supplemented with sodium deoxycholate, sodium lauryl sulfate, and 5 mM dithiothreitol. Sulfhydryl groups in cysteines were alkylated with 2-chloroacetamide to form carbamidomethyl. Overnight digestion was performed after adding 0.5 μg trypsin and $CaCl_2$. Detergents were removed/precipitated with Trifluoroacetic Acid and the digest washed twice with ethylacetate. Desalting of the protein sample was performed on a C18 solid phase extraction column ("home-made ZipTip") and after purification proteins were solubilized in 3% Acetonitrile and 0.5% Formic acid. A fraction of each sample was injected on a 20cmx100μm ID C18 column with an EASY-nLC 1000 liquid-chromatograph coupled to a Thermo Scientific Orbitrap Fusion Tribrid mass spectrometer. Statistical significance data analysis of MS and MS/MS spectra was done with the Mascot software (Matrix Science). These experiments were performed at the proteomics core facility of the Erasmus MC Rotterdam.[11]

Antibodies

Primary antibodies used include polyclonal rabbit anti-human SMPD4 (SP0281, ECM biosciences, ICC 1:500, WB 1:1,000), monoclonal rabbit anti-human CNX (C5C9, Cell signaling, ICC 1:50), mouse monoclonal anti-Myc (9B11, Cell signaling technologies, ICC 1:500), anti-LC3B (2775S, Cell signaling, ICC 1:100), rabbit polyclonal anti-LC3B (L7543 Sigma Aldrich WB 1:1,000),

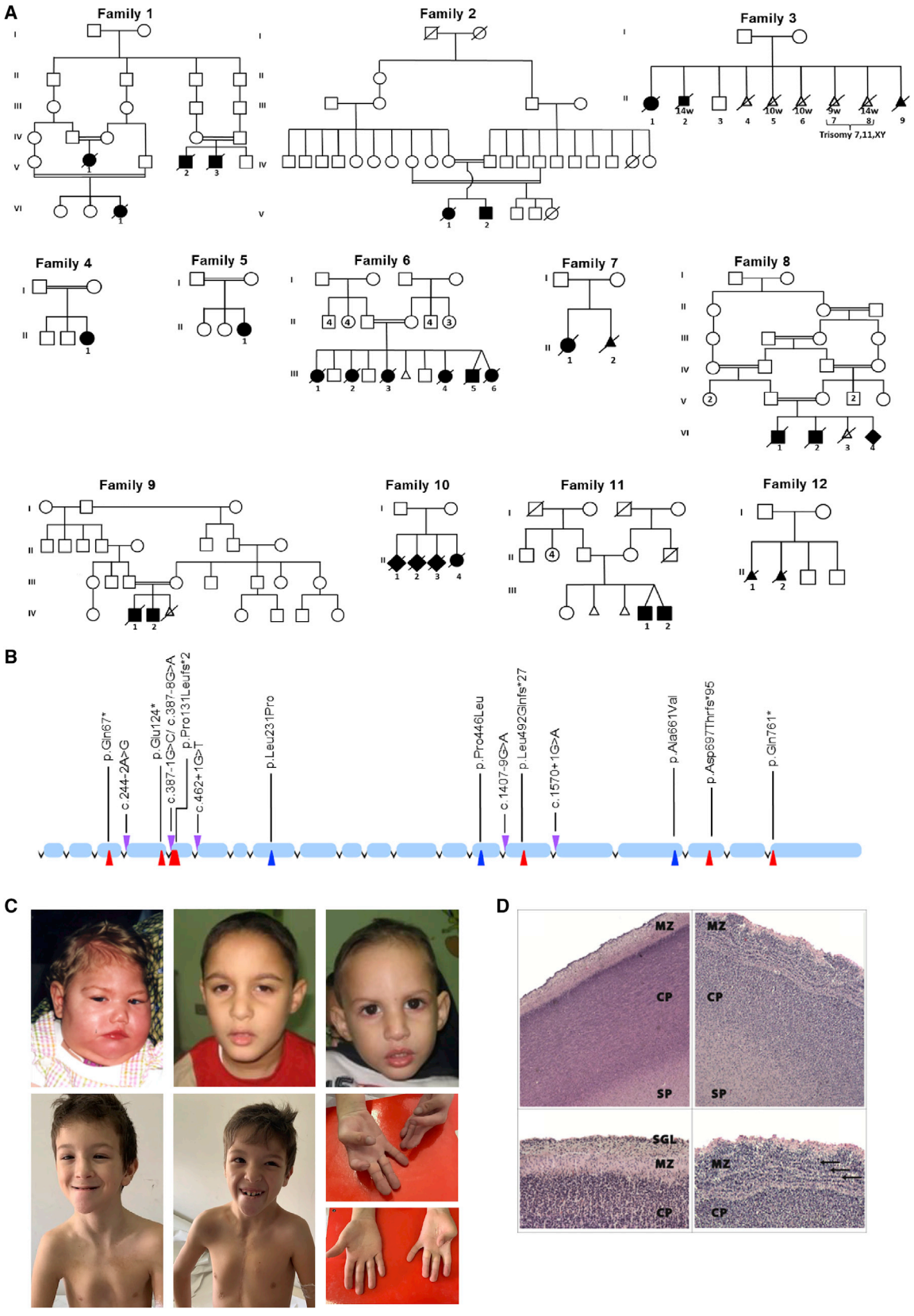

Figure 1. Clinical Phenotype of Individuals with *SMPD4* Variants

(A) Pedigrees of the 12 families (affected individuals are black symbols). From 21 individuals we obtained both clinical data as well as confirmation of variants in *SMPD4*. Subjects II-2/9 Fam 3, III-1/2/3/4 Fam 6, VI-1/4 Fam 8, and II-1/2/3 Fam 10 presented with similar clinical features but no extensive clinical reports are available. For 2 of them (Fam 3 II-9 and Fam 8 VI-1), variants in *SMPD4* were confirmed by sequencing.

(legend continued on next page)

rabbit polyclonal Anti-Beta_actin (Genetex WB 1:1,000), and mouse monoclonal anti-414 covans MMS-120P (Biolegend, ICC 1:500).

Secondary antibodies used include: Green goat anti-Rabbit (IgG) Alexa fluor 488 (1:400, Thermo fisher scientific, A110888), Red Cy3 affiniPure Donkey Anti-Mouse IgG (1:100, Jackson Laboratories, 715-165-150). Secondary antibodies used for WB: Red IRDye 680RD Goat anti-Rabbit IgG (H + L) (LI-COR Biosciences, 926-68071, 1:10,000)

Western Blot

Protein lysates were freshly prepared or thawed on ice and diluted in 4 × Laemmli buffer with bromophenol blue to equal amounts of total protein (10–30 μg loaded). Proteins were separated on a 4%–15% Criterion TGX Stain-Free Protein Gel in a Criterion Cell geltank (Bio-Rad Laboratories) at 200 Volt for 45 min in Tris-Glycine-SDS running buffer. Proteins were transferred to a nitrocellulose membrane (Amersham Protran 0.45 NC, GE Healthcare Life Sciences) for 20 min at 2.5A and 25V. After antibody incubation bands were detected with a fluorescent-based approach on the Odyssey Infrared Imager (LI-COR Biosciences).

Immunofluorescence of Exogenous SMPD4

HEK293T cells transfected with Myc-SMPD4 were fixed with methanol for 10 min at −20°C. Samples were blocked and permeabilized in blocking buffer (50 mM Tris HCl [pH 7.4], 0.9% NaCl, 0.25% gelatin, 0.5% Triton X-100) for 90 min on ice. Primary antibodies were dissolved in blocking buffer. Sections were incubated overnight at 4°C. The next day slides were washed three times with PBS and incubated with the secondary antibodies for 1 h at room temperature. Coverslips were mounted with DAPI containing Prolong Gold and dried at 37°C.

LC3B Autophagy

Fibroblasts were fixed and permeabilized in 3.7% (w/v) formaldehyde in PBS and 0.1% (v/v) Triton X-100 in PBS, subsequently, preceeded by PBS washes. Antibodies against LC3B, with high specificity for the LC3B-II isoform, were diluted in PBS/1% non-fat milk (BIO-RAD). Actin was detected with Texas Red conjugated phalloidin. Specimen were mounted in PreserveGold mounting medium. Total cytosolic intensity and number and size of LC3B-II-positive punctae were quantified, by analysis of particles with circularity 0.5–1.0. The distribution of particle sizes was plotted. Control: n = 598; fibroblasts from individuals with *SMPD4* variants: n = 928 (log transformed for better distribution). Calculated p value (one sided Mann-Whitney U test).

Detection of Activated Caspases

Active caspases-3/7 were detected using FAM-FLICA Caspase-3/7 activity kits (ImmunoChemistry Technologies). Fibroblasts from affected individuals and healthy control subjects were plated in a concentration of 7.5×10^4 cells on 24 mm coverslips and cultured in 2 mL DMEM with serum. After 24 h culture media was replaced with 2 mL DMEM without serum. The next day, cells were treated with 0.1 mM hydrogen peroxide for 24 h to induce apoptosis. Following hydrogen peroxide treatment, 300 μL 30× FAM-FLICA Caspase-3/7 solution was added to the cultures at a ratio of 1:30 for 1 h at 37°C and 5% CO_2. Cells were washed with DMEM with serum, stained with Hoechst, and fixed according to manufactures' protocol. Caspase-positive cells were counted on a Zeiss Imager Z1 with AxioCam3.2.8 MRm fluorescence microscope.

Light Fluorescent Microscopy

Confocal fluorescent Z stack images were acquired with the Broadband Leica TCS SP5, using Leica LAS AF application (Leica Microsystems). Lasers with 405 nm, 488 nm, and 561 nm excitation wavelength were used to visualize blue, green, and red fluorescent secondary antibodies. Maximal projection of Z stack images were processed with Fiji ImageJ software.

Statistics

Statistical tests were performed with Prism 5 GraphPad Software and are specified in legends of the experiments. All error bars represent the standard error of the mean (SEM), unless otherwise specified in the legend.

Results

Identification of *SMPD4* Bi-allelic Variants in Affected Children

Exome sequencing was performed in probands from 12 unrelated families and detected candidate homozygous or compound heterozygous variants in *SMPD4* in 12 individuals. In total, 32 individuals from the 12 families presented with a similar distinctive phenotype. Follow-up Sanger sequencing on affected family members who were available for sequencing summed up to 23/32 genetically confirmed diagnoses (Figure 1, families 2–12; Table 1). In the only family where initially no variants could be detected by exome sequencing (family 1, Figure 1), SNP arrays were performed on four affected individuals from three sibships in the same large consanguineous pedigree. Only one shared region of homozygosity (ROH) on chromosome 2q14–2q22 (GRCh37 chr2:123202031–138700836) was identified. *SMPD4* was the only gene within this ROH showing expression anomalies in RNA-seq analysis which was carried out on transcripts obtained from fibroblasts of individual V-3 and VI-1 and four age- and gender-matched control subjects

(B) Schematic overview of *SMPD4* variants (GSDS 2.0). Red arrowheads, truncating variants; purple, intronic splice variants; blue, missense variants.
(C) Upper panel: facial features of subject II-1 from family 3 (left), and older IV-1 (middle) and younger IV-2 (right) affected siblings of family 9. Lower panel: facial features of subject III-2 (left) and III-1 (middle) of family 11. Contractions of the distal joints of the upper limbs of subject III-1 (upper) and III-2 (lower) of family 11.
(D) Cerebral cortex during gestation. Upper left panel: normal cerebral cortex at the 20th week (hematoxylin and eosin staining, magnification 4×). Upper right panel: cerebral cortex in *SMPD4* fetal brain from individual II-2 (family 7) at 22w gestation (cresyl violet staining, magnification 4×). Lower left panel: Normal molecular zone at the 20th week (hematoxylin and eosin staining, magnification 10×). Lower right panel: Molecular zone in *SMPD4* case (cresyl violet staining, magnification 10×). Clusters of cells forming dense groups bordering on pial surface and waves of over- migrating neurons (marked with arrows) that disrupt the marginal zone. Lack of subpial granular layer. Marginal zone (MZ), cortical plate (CP), subplate (SP), subpial granular layer (SGL).

Table 1. Summary of *SMPD4* Genomic Variants

Family	Zygosity	Genomic Position (hg19; GRCh37)	cDNA Position (NM_017951)	Protein Position	Variant Type	Frequency (gnomAD)	CADD Score	mRNA Prediction
Family 1	homozygous	g.130912841C>T	c.1407−9G>A	p.?	splice region	0.00001629	10.92	RNA-seq revealed 3 alternative transcripts: (1) a newly created splice acceptor site due to the variant at position c.1407–7 leading to a frameshift, (2) usage of a wild-type internal splice site at position c.1423, (3) unspliced transcripts where intron 14 remains unspliced
Family 2	homozygous	g.130912668C>T	c.1570+1G>A	p.?	splice site	none	29.4	alteration of the WT donor site, most probably affecting splicing
Family 3	compound heterozygous	g.130930851C>A	c.462+1G>T	p.?	splice site	0.000004068	26.1	alteration of the WT donor site, most probably affecting splicing
	compound heterozygous	g.130932531G>A	c.199C>T	p.Gln67*	nonsense	none	36	null
Family 4	homozygous	g.130910448G>A	c.2281C>T	p.Gln761*	nonsense	none	39	null
Family 5	homozygous	g.130930908_130930924del	c.390_406del	p.Pro131Leufs*2	deletion	none	32	null
Family 6	homozygous	g.130931231T>C	c.244−2A>G	p.?	splice site	0.00003255	26.2	alteration of the WT acceptor site, most probably affecting splicing
Family 7	compound heterozygous	g.130930006A>G	c.692T>C	p.Leu231Pro	missense	none	23.5	deleterious by SIFT disease causing by MutationTaster
	compound heterozygous	gene deletion, 2q21.1 deletion (g.129 829 959 - 131 404 737)						null
Family 8	homozygous	g.130931103C>A	c.370G>T	p.Glu124*	nonsense	none	37	null
Family 9	homozygous	g.130913677G>A	c.1337C>T	p.Pro446Leu	missense	0.00002549	25.5	deleterious by SIFT, disease causing by MutationTaster
Family 10	homozygous	g.130912760_130912766del	c.1473_1479del	p.Leu492Glnfs*27	deletion	none	33	null
Family 11	compound heterozygous	g.130911303G>A	c.1982C>T	p.Ala661Val	missense	0.00003187	26.2	tolerated by SIFT, disease causing by MutationTaster
	compound heterozygous	g.130930935C>T	c.387−8G>A	p.?	splice site	0.0007863	0.916	alteration of the WT acceptor site, most probably affecting splicing
Family 12	compound heterozygous	g.130910946del	c.2088del	p.Asp697Thrfs*95	deletion	0.000007958	24.9	null
	compound heterozygous	g.130930928C>G	c.387−1G>C	p.?	splice site	0.000004009	26	alteration of the WT acceptor site, most probably affecting splicing

(Figures 2A and 2B). Detailed evaluation of *SMPD4* transcripts in affected individuals revealed an intronic variant (GRCh37 chr2:130912841C>T chr2:130155268C>T; GenBank: NM_017951; c.1407−9G>A), which was filtered out by bioinformatic pipelines applied to exome sequencing data, being beyond the intronic limits usually considered in the analysis (±5 bp from exon border). The variant was retrospectively found in the whole-exome sequencing data.

In total, 16 different novel or ultra-rare (minor allele frequency $\leq 1.0e^{-4}$) *SMPD4* variants were identified in 12 unrelated families. The databases used for determining the frequency of all variants are specified for each family in the Supplemental Results. Most of them were predicted to have loss-of-function effects (six splice sites, four nonsense variants, two intragenic variants, and one whole gene deletion), and only three were missense changes with damaging potential according to their Combined Annotation Dependent

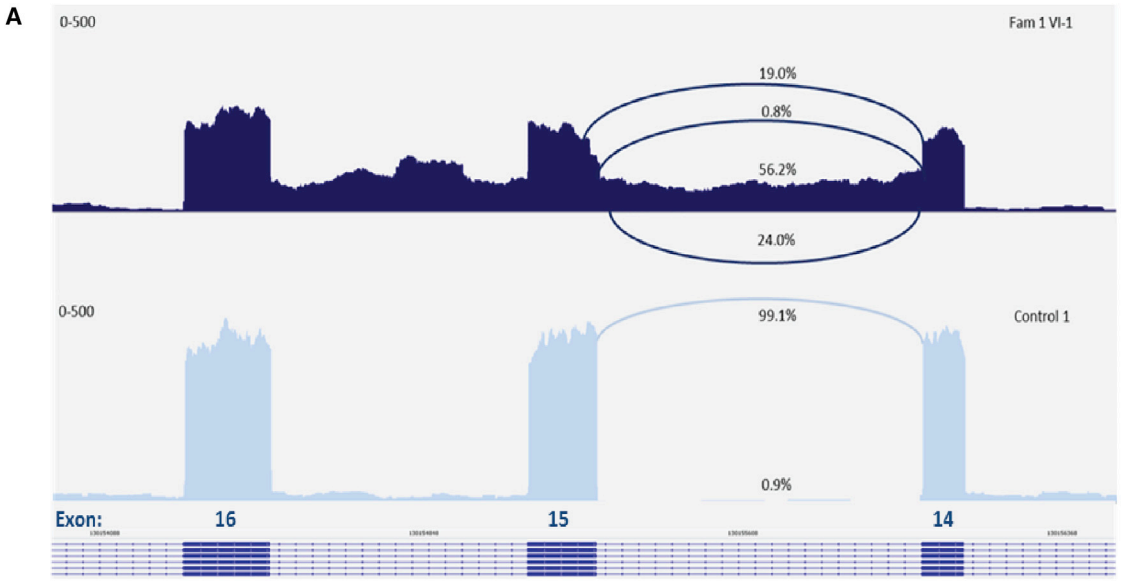

B

Percentage of transcripts						
	WT splice acceptor	Mutant splice acceptor (exon 15+8nt)	Internal splice acceptor (exon 15-16 nt)	Unspliced	Total	% of reads relative to controls
Control 1	99.1	0.0	0.0	0.9	100.0	130.5
Control 2	98.7	0.0	0.0	1.3	100.0	85.5
Control 3	99.6	0.0	0.0	0.4	100.0	99.4
Control 4	99.2	0.0	0.0	0.8	100.0	84.5
Fam1 V-3	1.4	34.5	12.9	51.1	100.0	37.2
Fam 1 VI-1	0.8	24.0	19.0	56.2	100.0	37.1

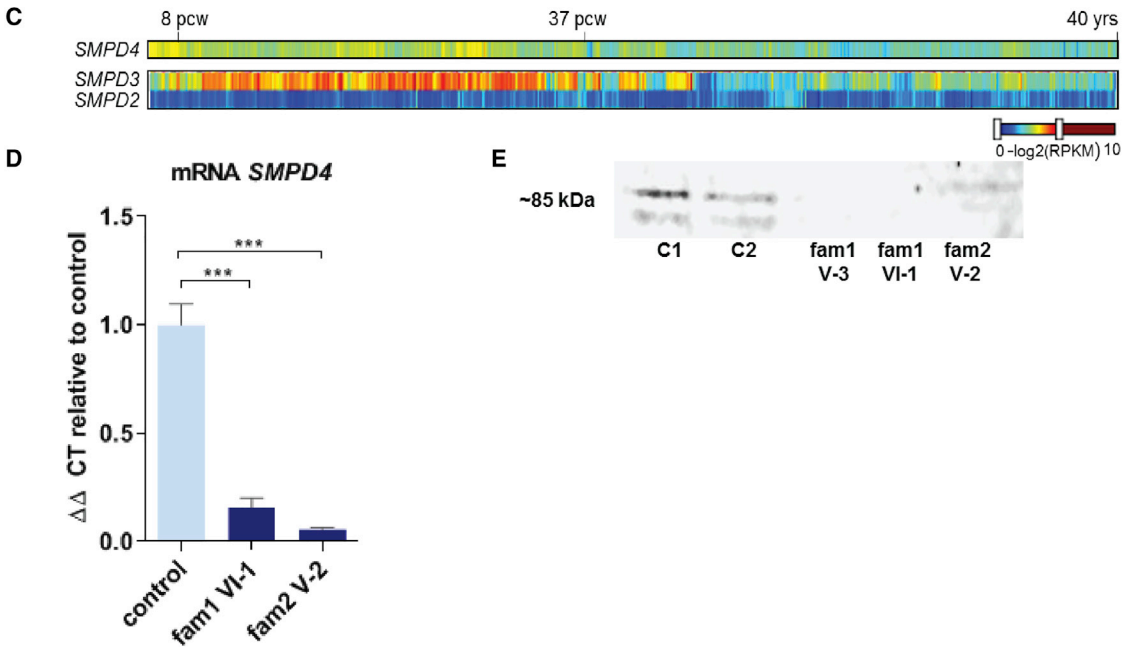

Figure 2. Transcriptome Analysis and Quantification of *SMPD4* mRNA Expression and Protein Levels

(A and B) Graphic illustration (adapted from IGV Sashimi plot) (A) and table of the percentage (B) of *SMPD4* transcripts in RNA-seq data of total RNA of individuals Fam 1 V-3 and VI-1 and 4 control individuals. RNA-seq reads are normalized to counts/billion, percentages are calculated for each transcript compared to the total *SMPD4* (wild-type and alternative) transcript counts (GRCh38).

(C) Allen human brain atlas: expression of nSMases during pre- and postnatal development. Higher expression of *SMPD4* in the first 8 weeks post conception (pcw) compared to other nSMases (see Allen Brain Atlas in Web Resources).

(D) *SMPD4* mRNA expression in fibroblasts from two probands (family 1, VI-1 and family 2, V-2). Unpaired t test with Welch's correction, two-tailed, n = 2 experiments, 4 independent control cell lines were used.

(E) Western blot of SMPD4 in fibroblast homogenate from three individuals with *SMPD4* variant (Family 1, VI-1, family 1, V-3 and family 2, V-2) versus two control subjects (C1, C2).

Table 2. Phenotype of Affected Individuals with *SMPD4* Variants

Disease Manifestation	Number of Individuals with Bi-allelic *SMPD4* Variants[a] (n = 21)	Percentage of All Assessed Individuals
Growth Parameters and Survival		
IUGR	12/19	63.2%
Primary microcephaly	15/21	71.4%
length (<−2.5 SD at birth)	6/11	54.5%
Prenatal demise	3/19 terminated pregnancy	5.3%
Prematurity	7/18	38.9%
Death in infancy (<1 year of age)	6/18	33.3%
Neonatal respiratory distress	14/17	82.4%
Clinical Features		
Progressive microcephaly[b]	9/10	90%
Seizures	10/17	58.8%
Persistent respiratory distress[c]	11/18	61.1%
Congenital arthrogryposis	17/20	85%
Developmental delay	7/7	100%
Facial dysmorphisms	15/15	100%
Congenital heart defect	12/21	57.1%
Diabetes mellitus	2/19	10.5%
Muscular tone		
Hypotonic	4/15	26.7%
Hypertonic	9/15	60%
Normotonic	2/15	13.3%
MRI		
Simplified gyration[d]	12/18	66.7%
Thin corpus callosum	9/20	45%
Hypomyelination	7/19	36.8%
Cerebellar hypoplasia	10/21	47.6%
Brainstem hypoplasia	3/20	15%

[a]The number individuals *SMPD4* variants and detailed clinical information available
[b]Defined as >0.5 SD OFC decline after birth
[c]Including persistent stridor, laryngomalacia, and oxygen desaturations
[d]In two individuals, lissencephaly was reported, but MRI was not revised by the authors

Depletion (CADD) Phred score ≥ 20.[12] All *SMPD4* variants were validated and their segregation within families was verified through Sanger sequencing (Figure 1B; Table 1).

Clinical Features

Clinical and neuroimaging data are available for 21 of the 32 individuals affected by a similar neurological phenotype (Figure 1A, Tables 2 and S2). Of 11 individuals, no extensive clinical descriptions are available. Details on case reports are illustrated in the Supplemental Note and are summarized in Table S2.

The majority of affected infants presented with IUGR and/or congenital microcephaly or microcephaly at first examination, neonatal respiratory distress, often preventing weaning from assisted ventilation, congenital arthrogryposis of hands and feet, abnormal muscular tone, and structural brain abnormalities. Head occipital-frontal circumference (OFC) at birth ranged between borderline normal values at −2 SD up to −4.5 SD. All OFC measurements after birth report values between −2.5 and −9 SD. Preterm birth and low birth weight were common. All but four affected siblings from two families (family 9 and 11) shared this severe neonatal presentation and a substantial number of them (6/16) died in infancy. The two children from family 9 that presented with milder clinical manifestations at birth were the longest survivors and died at the age of 12 years (family 9, Figures 1A and 1C, Tables 1 and S2). Children surviving the neonatal period show severe developmental delay in motor skills and cognition, most of them show only head control, while the contractures appear to be permanent with limited spontaneous movements. Notwithstanding the severe neurodevelopmental disorder and the structural brain anomaly, epilepsy was not frequently reported. The longest surviving children from family 9 are reported to have suffered from focal or secondary generalized seizures, provoked by fever. The nine-year-old twins from family 11 never experienced epilepsy. It is remarkable that not a single individual has been reported with a well-described electroclinical epileptic syndrome and that some individuals deceased in early infancy are reported to have had no seizures and a normal EEG (e.g., family 1 and family 10). Occasional tonic-clonic seizures did occur in some individuals but did not play a major role in early demise. The major determinant of short survival in younger children were central hypoventilation and respiratory infections, while cardiomyopathy with heart failure were crucial only in the two subjects who survived after the first decade (family 9). Two siblings developed diabetes mellitus (family 2).

Neuroimaging at birth or in infancy was available for nine individuals and consistently showed microcephaly with a simplified gyral pattern and a normal or even thin cortical layer, a thin corpus callosum, delayed myelination, and in some cases mild cerebellar and brainstem hypoplasia (Figure 3). For two individuals, repeat MRIs were available, performed at the age of, respectively, 3 years (family 1, subject VI-1, at few hours postmortem) and 5 years (family 2, subject V-2). The repeat MRIs showed striking global hypomyelination, suggesting involvement of both neuronal and glial cell lineages in the disease process. Remarkably, the fetal MRI of subject II-2 of family 7 did not reveal any brain anomaly in the 20th week of gestation, indicating that microcephaly occurs (or can be detected) only in late pregnancy (Figures 3S–3V).

Pathological brain examination of the affected fetus in family 7 (II-2) revealed disorganization of cerebral cortex

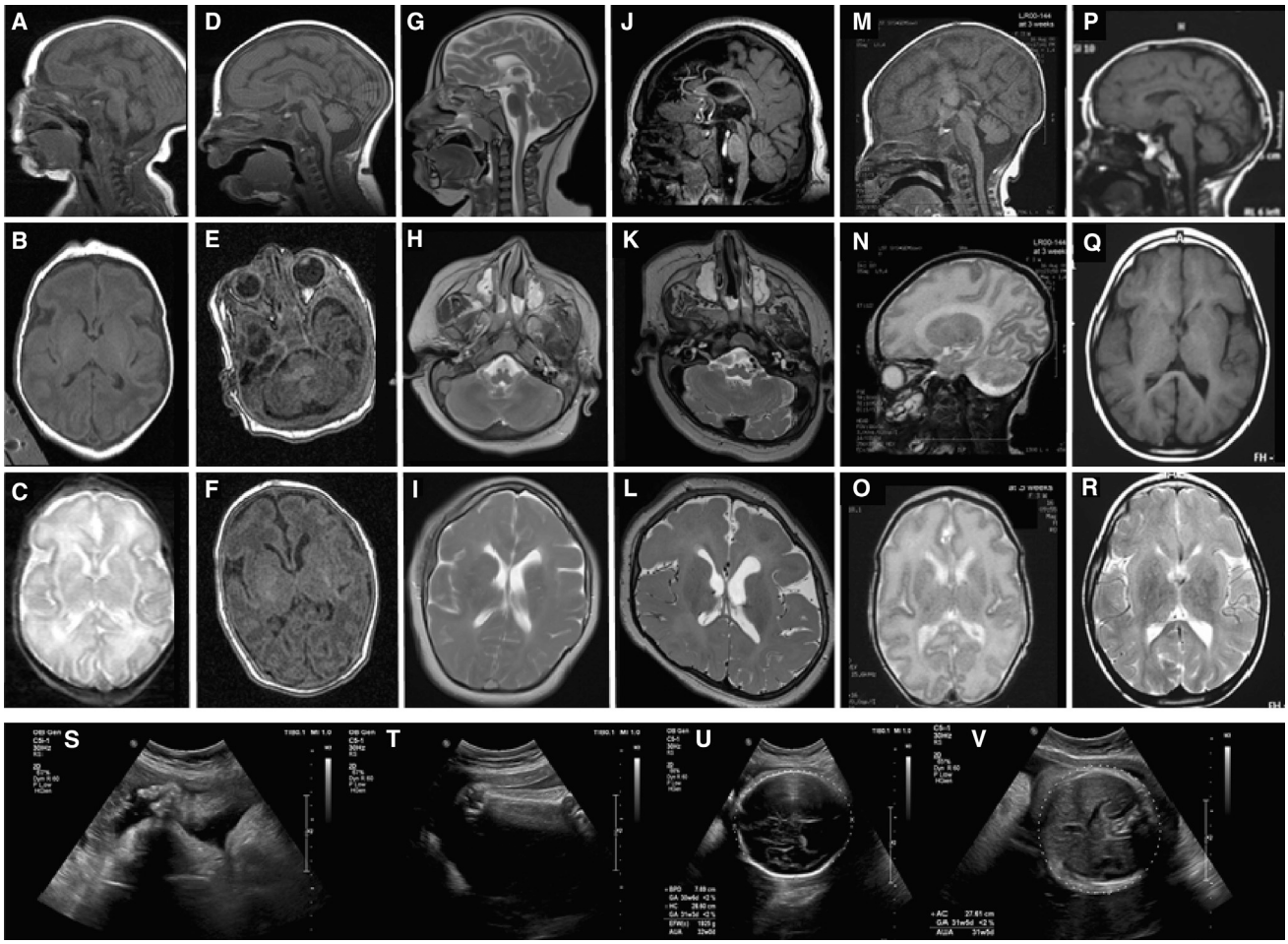

Figure 3. Brain Imaging and Prenatal Ultrasound of Affected Individuals
(A–C) Family 1, V-1 at term, T1 weighted images (A, B) and T2 weighted image (C) showing microcephaly (A), simplified gyral pattern (B, C), and insufficient myelination (C).
(D–F) T1 images of family 1, VI-4 at term, showing small vermis and simplified gyration.
(G–I) T2 weighted images, follow-up MRI of the same subject of family 1, VI-1 at 3 years, few h post-mortem, showing simplified gyration, brain stem hypoplasia and cerebral global hypomyelination.
(J–L) Family 2, V-2 (E-A) at 5 years, showing simplified gyral pattern, mild brain stem hypoplasia, thin corpus callosum and global hypomyelination in (L). Note the right parietal positional plagiocephaly.
(M–O) Family 3, II-1 (LR00-144) at 3 weeks, showing simplified gyration and delayed myelination on T2 weighted images (N and O).
(P–R) Family 9, subject II-2 at the age of 5 years, showing simplified gyral pattern and delayed myelination on T2 weighted images (in R).
(S–V) Family 10, subject II-4, prenatal ultrasound at 37 GW.
S, clenched hand; T, talipes; U, head circumference corresponding to GW 31+5; V, abdominal circumference corresponding to GW 31+5 (symmetrical IUGR).

architecture at the 22nd week of gestation. Interruption of the marginal zone was associated with overmigration of neurons forming thick clusters on the pial surface and along the axons of Cajal-Retzius neurons (Figure 1D). These data suggest, besides a general proliferation disorder (accounted for by the microcephaly with simplified gyral pattern) (Figure 3), also a global derangement of cortical structure.

Functional Analysis of SMPD4

Effect of Candidate Variants on SMPD4 Expression and Splicing Isoforms

Abundance and sequence of *SMPD4* transcripts were analyzed in affected individuals of families 1 (V-3 and VI-1) and 2 (V-2), for whom fibroblast cultures were available.

In family 1, quantification of uniquely mapped RNA-seq reads revealed a drastic (>99%) reduction of wild-type *SMPD4* mRNA and the production at low levels (37% of wild-type transcript in control subjects) of three aberrant transcripts which all are predicted to encode premature stop codons (Figures 2A and 2B). These isoforms use alternative splice acceptor sites, adding 7 intronic nucleotides or eliminating 16 exonic nucleotides, or leave intron 14 unspliced with reading frame loss. The latter transcript is weakly observed also in control subjects (0.4%–1.3%) but is the most abundant isoform in individuals with the c.1407−9G>A variant (>50%).

The strong reduction of *SMPD4* expression was confirmed in family 1 and demonstrated in family 2 at

both RNA and protein levels by qPCR and western blotting, respectively (Figures 2D, 2E, S1A, and S1B).

Expression data of *SMPD4* mRNA during human brain development were retrieved from Allen human brain Atlas. Compared to other nSMases, *SMPD4* is highly expressed during the first 8 weeks post conception through the fetal period, and then steadily decreases during postnatal life. Consistently, the Human Protein Atlas reports low levels of SMPD4 protein in the adult brain (Figure 2C).

Gene Expression Profiling and Connectivity Mapping

In order to understand the molecular function of SMPD4 and downstream effects of *SMPD4* depletion, we performed differential gene expression analysis by using RNA-seq data from individuals V-3 and VI-1 of family 1 and four age-matched control subjects. We identified 123 significantly upregulated genes and 27 downregulated genes (FDR < 0.05) (Table S3). Functional annotation clustering of differentially expressed genes (DEGs) with DAVID's standard set of gene ontology, pathway, functional category, disease, and protein domain terms yielded seven significantly enriched clusters (enrichment score > 1.3) (Figure S3).[13,14] Genes in these categories were both up- and downregulated. The most significant cluster (enrichment score 6.26) was dominated by terms related to protein secretory pathway, including signal peptide, secreted, and transmembrane region. Additional enriched terms were related to growth factor activity and embryo development, partly due to upregulation of growth factors (i.e., *BMP4* [MIM: 112262] and *FGF10* [MIM: 602115]) and HOXA and HOXB homeobox genes. Other significantly enriched clusters contained extracellular matrix and cell adhesion terms.

Consistently, investigation of the cellular and molecular functions of all DEGs by IPA revealed for cellular functions enrichment of genes involved in several cellular activities, such as movement, signaling, growth, proliferation, development, death, and survival (Table S4A). IPA of upstream regulators showed Tretinoin, a major player of retinoic acid (RA) signaling, and tumor necrosis factor (TNF) as the most significant upstream regulators suggesting aberrant RA and TNF signaling in SMPD4-depleted fibroblasts (Table S4B).

To further understand the effects of SMPD4 deficiency, we compared DEGs to the catalog of gene expression profiles reflecting chemical, genetic, or disease perturbations obtained at Broad Institute (L1000 connectivity mapping[15]). Interestingly, cells knocked down for *SPHK2* (MIM: 607092), encoding a sphingosine kinase directly involved in sphingomyelin homeostasis and sphingosine-1-phosphate (S1P) production, had the most closely related transcriptional profile to that detected in SMPD4-deficient cells (Figure S4).

Electron Microscopy and LC3B Immunofluorescence Staining Revealed RER Membrane Dilatation and Autophagy in SMPD4-Deficient Fibroblasts

Because of the prominent dysregulation of genes encoding proteins routed through the secretary pathway, we investigated possible ultrastructural alterations by electron microscopy in skin fibroblasts from individuals VI-1 (family 1) and V-1 (family 2) (Figures 4A and 4B). Compared to parallel ER stacks and granular content observed in age- and sex-matched control fibroblasts (black arrows in Figure 4A), the rough ER (RER) in fibroblasts from affected individuals was characterized by an extensive distribution of dilated cisternae (Figure 4A, black arrowheads) and a decrease of morphologically normal RER. Some of the dilated cisternae were partially or completely filled with a floccular material ascribable to aggregates of misfolded proteins (white asterisks), suggesting defective RER functioning. In addition, an increase of lysosomes (ly) and late autophagic vacuoles (white arrow) was detected, suggesting an activated autophagic process (Figures 4A, 4B, and S5A, Band C). The other cytoplasmic organelles appeared intact.

To confirm the presence of autophagic vesicles, we analyzed the localization of the LC3B-II autophagy marker in fibroblasts from affected individuals of family 1 (V-3 and VI-1). The experiments showed an increased number and size of cytoplasmic punctae, with a statistically significant increase of total cytosolic LC3B-II intensity compared to control subjects ($p = 1.7e{-}08$) (Figures 4C, 4D, S5B, and S5C). However, western blots of LC3B-II protein levels after starvation and inhibition of lysosomal degradation (e.g., chloroquine treatment) showed an only modest and not statistically significant increase of LC3B-II protein levels between control and SMPD4-deficient cells (Figures S5D and S5E).

Structural RER Membrane Alterations Do Not Correspond to Activation of UPR

Alterations in RER morphology and proteinaceous inclusions as observed by EM in fibroblasts from affected individuals are signs of ER stress, which often lead to activation of several intracellular signaling pathways known as the unfolded protein response (UPR).[16] Activation of the UPR is essential in alleviating ER stress and maintaining protein biogenesis, protein quality, and membrane integrity. To evaluate UPR activation in SMPD4-deficient fibroblasts, we quantified mRNA levels of UPR markers *CHOP* (MIM: 126337) and spliced *XBP-1* (MIM: 194355). Expression of these genes resulted to be similar in cells from affected individuals and age-matched control subjects, both in basal conditions and after tunicamycin treatment, which blocks N-glycosylation and induces dose-dependent expression of UPR genes (Figures S5F–S5I). These findings indicate that SMPD4 deficiency does not induce a constitutive activation of the UPR in cultured fibroblasts and does not alter the ability of cells from affected individuals to normally activate the UPR in response to ER stress *in vitro*.

SMPD4 Localizes to the Endoplasmic Reticulum and to the Nuclear Envelope

Co-localization experiments of overexpressed myc-tagged SMPD4 with the ER marker calnexin in HEK293T cells confirmed previously shown localization of SMPD4 to the peripheral ER membranes and the outer layer of the nuclear envelope (Figure 5A). Interestingly, co-staining with the nuclear pore complex (NPC) antibody mab-414 showed that a substantial part of the perinuclear SMPD4

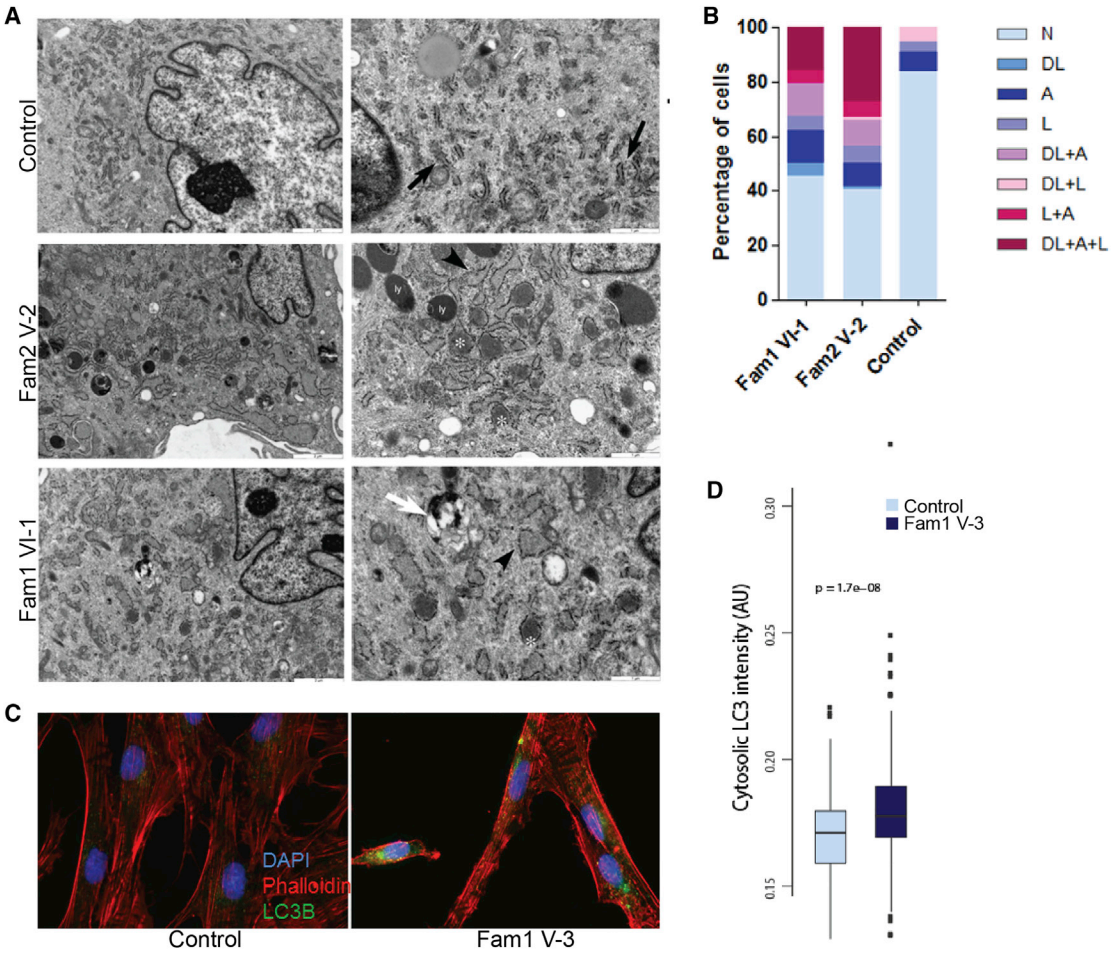

Figure 4. Electronmicroscopy of *SMPD4*-Mutated Fibroblasts and LC3B-II Immunofluorescence Staining
(A) Electron microscopy on fibroblasts from individuals with *SMPD4* variants and a control subject. Normal granular content of RER is indicated by black arrows in control fibroblasts. Cellular abnormalities in SMPD4-deficient cells include dilated RER cisternae (black arrowheads), with floccular material (white asterisks), increase of lysosomes (ly), and late autophagic vacuoles (white arrow).
(B) Quantification of electron microscopy findings; n, normal morphology; dl, dilated ER; A, increased number of autophagic vacuoles; L, increased number of lysomes ($n = 153$ cells, $p < 0.0001$ tested by the Fisher and the χ^2).
(C) Immunofluorescence staining shows increased LC3B-II signal in SMPD4-deficient cells. Phalloidin antibodies mark the actin cytoskeleton, DAPI staining the nucleus.
(D) Quantification of LC3B-II cytoplasmic fluorescence signals, one-sided Mann-Whitney U test.

localized close to NPCs (Figure 5A). We could not detect endogenous SMPD4 at immunofluorescence of cultured cells, either HEK293T or skin fibroblasts using commercially available antibodies.

We then focused on SMPD4 interacting proteins to elucidate its function and get some clues about the pathogenetic mechanism induced by SMPD4 deficiency. Immunoprecipitation of exogenous human Myc-tagged SMPD4 in HEK293T cells followed by mass spectrometry identified 254 significant interacting peptides (Mascot score > 40), which we tested for enriched GO terms and protein networks (Tables S5 and S6).

The DAVID platform, interrogated for most frequent cellular compartments among nSMase3 interacting proteins, revealed enrichment for membrane structures as the ER, the proteasome, and the nuclear pore complex (NPC) (Table S3A). Consistently, analysis of interacting protein networks through IPA pointed toward ER membrane proteins (DHCR24, CDIPT, STT3A, DDOST, RPN1, SPTLC1, SSR3) (Figure 5B, left hub). Interestingly, the main function of the interacting ER membrane proteins is post-translational processing of proteins, including N-linked glycosylation, that can be correlated to the altered expression of glycoproteins found by gene ontology analysis of DGEs. The second significantly enriched network included proteins involved in molecular transport, RNA trafficking, cellular assembly, and organization ($p = 1e{-}56$), involving also multiple components of the nuclear pore complex and the nuclear envelope (e.g., NDC1, TPR, SEC13 and NUP133, nup205 and nup93, XPO1, XPOT) (Figure 5B, right hub). These data confirm localization of nSMase3 to the ER and the nuclear envelope and demonstrate its interaction with nuclear pore complexes.

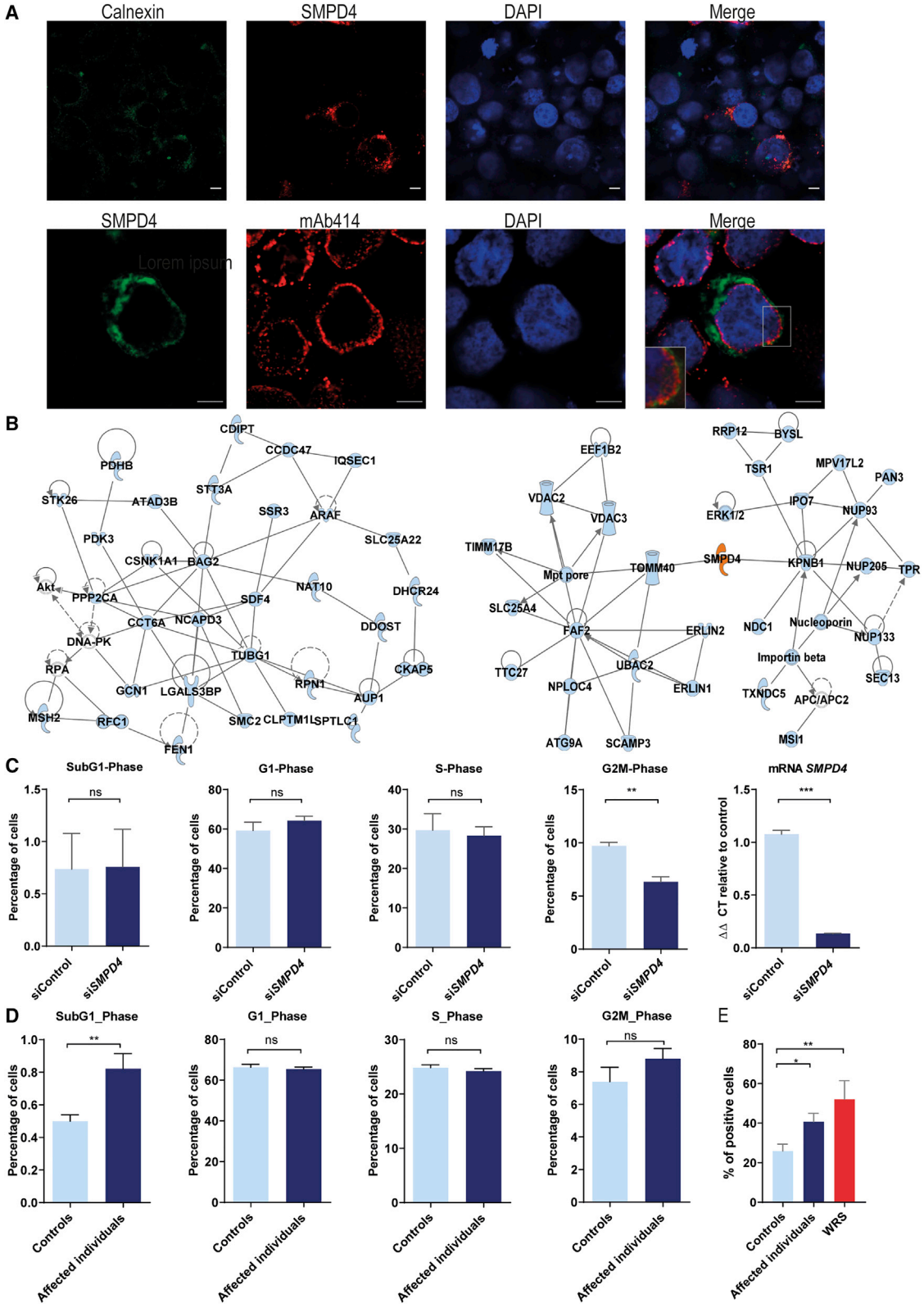

Figure 5. Cell Cycle Analysis and Subcellular Localization of SMPD4

(A) Immunofluorescence stainings of overexpressed Myc-tagged SMPD4 in HEK293T cells. The upper pannel shows localization of Myc-SMPD4 and the ER marker calnexin. The lower panel shows partial colocalization with the nuclear pore marker mab-414. Scale bar represents 5 μm. Partial zoom shows 300% enlargement.

(B) Network analysis by IPA (ingenuity platform analysis) of SMPD4 interactors. The proteins found by mass spectometry are depicted in blue. White nodes are connecting proteins not found by mass spectometry. SMPD4 is shown in orange. Solid lines indicate direct interactions, interrupted lines indicate indirect interactions. Network 1 (left hub) shows proteins of the endoplasmic reticulum, mainly

(legend continued on next page)

SMPD4 Loss Interferes with the Cell Cycle and Survival

Since previous studies have shown that downregulation of *SMPD4* by siRNA leads to mitotic failure in HeLa cells, and in view of the intriguing interaction of SMPD4 with NPC proteins, we evaluated the cell cycle in cultured fibroblasts from control subjects, after *siSMPD4*, and from affected individuals[17] (Figures 5C and 5D). We observed a significantly reduced percentage of *siSMPD4* cells in the G2/M phase (6.3%) compared to control subjects (9.71%, $p = 0.0013$, $t = 5.65$, $df = 6$), with a weak and not statistically significant increase of cells in the G1 phase, suggesting that knockdown of *SMPD4* in fibroblasts may lead to cell cycle delay at the G1 phase. However, fibroblasts from unrelated affected individuals did not show a delay in the G1 phase, but a consistent increase of cells at the subG1-phase ($p = 0.0041$, $t = 3.21$, $df = 22$), indicating enhanced apoptosis. Testing predisposition to apoptosis by detecting activated caspases in living cells after stress induced by hydrogen peroxide showed that fibroblasts from affected individulas are more susceptible to cell death than control subjects ($p = 0.015$, $t = 2.60$, $df = 35$) (Figure 5E).[18] These data indicate that human *SMPD4* mutant fibroblasts have a impairment during the cell cycle and are prone to apoptosis under stress conditions.

Discussion

We have identified an autosomal-recessive syndrome presenting with congenital microcephaly, arthrogryposis, severe neurodevelopmental delay, and early death in 12 unrelated families linked to bi-allelic *SMPD4* variants. Our observations shed light on an unanticipated and primary function of SMPD4 in brain development and in postnatal brain function.

SMPD4-Related Phenotypes

Primary, i.e., congenital microcephaly, is a genetically heterogeneous disorder often caused by variants in genes coding for proteins regulating cell cycle, e.g., centrosome assembly and duplication or mitotic spindle formation and orientation.[19–23] Many microcephaly subjects present with simplified gyration of the cerebral cortex, without overt structural anomalies, non-progressive intellectual disability, and normal life expectancy. However, another group of children presenting with congenital microcephaly is characterized by severe and progressive encephalopathy and early demise. This group includes disorders where brain imaging and post-mortem examination often show associated developmental defects and/or signs of degeneration of both the gray and white matter, such as hypomyelination and progressive atrophy. Almost all children with *SMPD4* variants identified in this study seem to share this second complex microcephaly phenotype. Brain pathology of an affected fetus (family 7, II-2) shows abnormal architecture of the cortex, similar to overmigration defects observed in cobblestone malformations, indicating abnormal interaction with Cajal-Retzius neurons and marginal zone components.[24] Additionally, in both cases where a repeat MRI was available (Figures 3G–3L), a global myelination defect was documented. Genetic disorders combining congenital or progressive microcephaly with hypomyelination are listed in Table S7 and share the severe clinical course as observed in *SMPD4*-affected individuals. Some disorders included in Table S7, like Vici syndrome (MIM: 242840) and *VPS11* variants (MIM: 616683), are linked to abnormal regulation of autophagy and autolysosome biogenesis, but are not related to sphingolipid metabolism. The presentation of the *SMPD4* variant phenotype with microcephaly, simplified gyral pattern, and congenital contractures is reminiscent of cerebro-oculo-facio-skeletal syndrome (COFS [MIM: 609413/216400]), a syndrome with congenital microcephaly caused by DNA repair defects (Table S7) or the recently described *SEC31A* (MIM: 610257) variant syndrome.[19,25] COFS was in fact the first suspected diagnosis in many of our case subjects, but the absence of cataract is unusual for COFS and DNA repair tests in cultured fibroblasts from affected individuals have repeatedly shown to be normal (G.M.S.M. and F.W.V., unpublished data).

SMPD4 is ubiquitously expressed in the body, but at lower level in the CNS during adulthood. Instead, RNA expression of *SMPD4* in brain appears to be the highest during embryonic and fetal development, leveling off after birth. It is possible that SMPD4 deficiency affects common pluripotent progenitors and/or leads to arrest of lineage maturation, hence causing a prevalent CNS phenotype.

Phenotype-Genotype Correlation

Most *SMPD4* variants (nonsense, frameshift, or affecting splice sites) were predicted to abolish or strongly reduce protein production, as demonstrated in fibroblasts from affected subjects of families 1 and 2, compatible with a loss-of-function pathogenetic mechanism. Notably, the intronic variant of family 1, which was missed by exome

involved in post-translational modifications ($p = 10e{-}62$). The right network hub shows multiple components of the nuclear pore complex ($p = 10e{-}56$). p values are calculated from the network score computed by IPA (Score = -log(Fisher's extract p value)).
(C and D) Flow cytometry of control fibroblasts after downregulation of *SMPD4* expression by siRNA ($n = 3$ experiments, unpaired t test, two tailed) (C) and fibroblasts from control subjects and three individuals with *SMPD4* variants (D). G1, S, and G2/M indicate cell cycle phases. The fifth upper graph indicates the level of *SMPD4* downregulation achieved.
(E) Susceptibility of cultured fibroblasts from individuals with *SMPD4* variants to apoptosis when treated with 0.1 mM hydrogen peroxide in comparison to control cell lines, using the FAM-FLICA Caspase-3/7 activity kits. All three available fibroblasts cell lines from SMPD4-affected individuals and two control cell lines were used ($n = 3$ experiments, $p = 0.015$, $t = 2.60$, $df = 35$, unpaired t test with Welch's correction, two tailed). Fibroblasts from one individual with Wollcot Rallison syndrome (WRS) were used as a positive control (unpaired t test with Welch's correction, two tailed, $p = 0.0013$, $t = 5.65$, $df = 22$). On the y axis: percentage of fluorescent cells.

sequencing, underscores the relevance of RNA-seq as gene discovery tool for homozygous loss-of-function variants in consanguineous pedigrees.

Three missense changes were identified, all predicted to have damaging but unexplored effects on SMPD4 protein, that could have altered function, structure, or stability. The homozygous p.Pro344Leu variant was found in the longest surviving children of family 9, who developed motor skills such as independent walking, unlike individuals with biallelic truncating variants, suggesting the persistence of residual SMPD4 function. Any clinical benefits of a possible residual function associated to the second missense change (p.Leu231Pro) in family 7 are probably hampered by the complete absence of the other allele, due to a contiguous gene deletion involving the entire *SMPD4* sequence. At the (neurological) mildest end of the spectrum, the twins of family 11 have microcephaly, arthrogryposis, and pectus excavatum, stature within the normal range, an important congenital heart disease, and only a mild intellectual disability. Their MRI scans do not show simplified gyration, one of them showing signs of perinatal asphyxia with cortical infarcts. Notably, the c.387−8G>A variant in these subjects has a lower CADD score, indicating the relative milder splice anomaly, hence the possibility of higher percentage of normal transcript.

ER Stress and Autophagy

SMPD4 encodes the putative neutral sphingomyelinase-3, localizes to the ER membranes and the Golgi apparatus, but its biological functions are poorly defined.[4,6] The protein has also been identified as NET13 in studies of the nuclear envelope composition.[7,8] Interestingly, studies on SMPD4 until now have ignored its presence in the outer nuclear envelope, and vice versa, studies on NET13 have not made a link with its presence in the ER.[6–8] The only study linking SMPD4 to mitosis is showing a delayed cytokinesis after siRNA treatment in HeLa cells.[17] We demonstrate that loss of SMPD4 leads to distinctive cellular dysfunctions that have previously been linked to the molecular pathogenesis underlying microcephaly, both related to ER and nuclear envelope.

Fibroblasts from affected children show RER structural abnormalities and an increase of autophagosomes. Investigating the localization of the autophagy marker LC3B-II shows an increase at immunocytochemistry experiments, although protein levels of this marker on western blot were not resolutive. Both the RER abnormalities as well as autophagy are linked to ER stress. ER stress, induced by genetic alterations or virus infections, has previously been implicated in microcephaly pathogenesis.[25–27] In mouse embryonic stem cells, ER stress promotes accelerated neuronal differentiation of the pluripotent and glial progenitor pools which can lead to microcephaly and global hypomyelination, both features observed in the affected children in our cohort.[28,29]

Cells with ER perturbations usually activate concomitant signaling pathways, including the most studied UPR, to restore homeostasis.[16] However, expression levels of canonical UPR regulators (*CHOP* and spliced-*XBP1*) in SMPD4-deficient fibroblasts resulted similar to control subjects, excluding the aberrant activation of this stress response *in vitro*. Possibly, fibroblasts are not the appropriate cell type since cells rapidly adapt to chronic stress by attenuating UPR signaling or inducing different cellular pathways after initial UPR activation through transient increased expression of these genes.[30,31]

In SMPD4-deficient fibroblasts, we observed signs of autophagy, which is an emerging ER stress effector pathway, preventing apoptosis.[32] Interestingly, the most significant upstream regulators of differentially expressed genes in fibroblasts from affected individuals were TNF, a known mediator of cellular stress and regulator of *SMPD4* expression, and all-trans retinoic acid, which is crucial during development of central nervous system and has stimulatory effects on autophagy.[33–35] The increased activation of caspases 3 and 7 leading to apoptosis in SMPD4 variant cells indicates that autophagy is not sufficient to compensate for SMPD4 loss and to prevent apoptosis *in vitro*.

Consistent with SMPD4 localization and function in the ER, RNA-seq analysis of fibroblasts lacking SMPD4 shows dysregulation of genes involved in the secretory pathway. Connectivity mapping also suggests functional correlations with proteins involved in sphingolipid metabolism, like SPHK2. This protein and its reaction product S1P are involved in regulation of cell growth, differentiation, migration, and survival as well as in assuring a correct embryo development, including brain morphogenesis.[36–39] Recently, variants in *SGPL1* (MIM: 603729), involved in S1P degradation, have been reported to cause severe brain malformations including microcephaly with simplified gyral pattern, underdeveloped frontal and temporal lobes, and cerebellar hypoplasia, along with severe congenital nephrotic syndrome. Increased autophagy due to alterations in S1P levels was proposed as the underlying pathogenetic mechanism.[40] Preliminary lipidomics analysis of cellular sphingolipids in cultured fibroblast homogenates did not show significant abnormalities in SMPD4-deficient cells, compared to control subjects (G.M.S.M. and M.F., unpublished data). Additional studies are needed to elucidate whether SMPD4 is relevant in the regulation of metabolic intermediates such as S1P.

SMPD4 Cellular Localization and Cell Cycle Investigation

Variants in several genes encoding key players of the mitotic process have been described in subjects with congenital microcephaly, implicating cell cycle alterations in the pathogenesis of this disorder.[19,20] Sphingolipids are also implicated in cell cycle regulation and *SMPD4* knockdown in HeLa cells causes defects in actin cytoskeleton leading to metaphase delay during mitosis, aberrant cytokinesis and cell division failure.[17] In the present study, cell cycle investigations indicated mitotic defects and susceptibility to apoptosis in native SMPD4-deficient cells and analysis of biological and molecular functions of DEGs in fibroblasts from affected individuals revealed

enrichment for genes involved in cellular growth, supporting a role of SMPD4 in cell cycle regulation.

We demonstrated that SMPD4 localizes both in the peripheral ER and the outer membrane of the nuclear envelope, with several interacting proteins belonging to the nuclear pore complex, involved in mitosis in higher eukaryotes, when the nuclear envelope breaks down and nuclear pore complexes disassemble.[41] One of these SMPD4 interactors, nucleoporin 133 (NUP133) is reported to be involved in cell cycle and its downregulation alters nuclear pore composition and disrupts neural differentiation in a mouse model.[42–45] Recently, a *NUP133* homozygous variant has been identified in a single family with Galloway-Mowat syndrome (GAMOS), characterized by microcephaly, brain anomalies, and early-onset nephrotic syndrome.[46] GAMOS-like families were found to have bi-allelic variants in *NUP107* (MIM: 607616), encoding a binding partner of NUP133. Disruption of mitotic processes during neuronal and glomerular development is considered a possible pathogenetic mechanism.[47] Since remodeling of the entire nuclear envelope is essential for dynamic changes of the nuclear architecture at different stages of the cell cycle and during cell differentiation, we hypothesize that absence of SMPD4 could interfere with the ability of the membrane to adapt during the cell cycle or with proper anchoring of the NPC in the membrane, leading to delay in the G1-phase observed after knock-down of *SMPD4* in fibroblasts.[48]

Conclusion

Loss of SMPD4 is associated with a severe neurodevelopmental disorder characterized by microcephaly, simplified gyration, hypomyelination, thin corpus callosum, mild cerebellar hypoplasia, brainstem hypoplasia, congenital arthrogryposis, diabetes mellitus, heart disease, severe encephalopathy, and respiratory problems often leading to early demise. We provide evidence that SMPD4 loss induces ER stress, autophagy, and interference with sphingolipids homeostasis. SMPD4 is a putative integral membrane protein that we showed to localize to both ER and the outer nuclear envelope. Cells depleted of SMPD4 by natural variants or by siRNA show mitotic abnormalitites and increased susceptibility to apoptotic cell death. The disease pathogenesis can be linked to all of the abnormalities observed *in vitro*. Interestingly, preliminary studies indicate that disruption of nSMase3 through knock out of murine *Smpd4* leads to partial lethality, while surviving mice show severe post natal growth retardation.[49] Future studies in appropriate models are needed to address the intriguing link between regulation of ER stress, cell division, and association with nuclear pore proteins, in order to unravel this interesting sphingolipid-related pathway leading to the severe human cerebral developmental disorder.

Accession Numbers

The accession number for the RNA sequencing data reported in this paper is Gene Expression Omnibus: GSE133264.

Supplemental Data

Supplemental Data can be found online at https://doi.org/10.1016/j.ajhg.2019.08.006.

Acknowledgments

We thank Mark Nellist, Niels Galjart, Danny Huylebroeck, Robert W. Hofstra, and Andreas Kremer for fruitful discussions and continuous support. G.M.S.M. is supported by ZonMW Top grant #91217045 and by private donations. Research reported in this publication was supported by the National Institute of Neurological Disorders and Stroke (NINDS) under award number K08NS092898 and Jordan's Guardian Angels (to G.M.M.). We thank the Broad Institute (U54HG003067 to E. Lander and UM1HG008900 to D. MacArthur). R.W.S. is supported by the NIH (R01NS085023). We thank Lauren Blizzard with assistance in Sanger Sequence verification of affected individuals in family 8. We also thank Luisa Iommarini, Department of Pharmacy and Biotechnology-FABIT, University of Bologna, Bologna, Italy, for help with the LC3B western blots. W.W. was supported by a grant from National Science Centre, Poland 2015/19/B/NZ2/01824. A.C.J. is supported by a fellowship from FWO. A.C.J., G.M.M., G.M.S.M., M.W., M.S.Z., and W.B.D. are members of the European Network on Brain malformations (COST Action CA16118, https://www.cost.eu/actions/CA16118/).

Declaration of Interests

The authors declare no competing interests.

Received: May 7, 2019
Accepted: August 15, 2019
Published: September 5, 2019

Web Resources

Allen Brain Atlas, http://human.brain-map.org/
Connectivity mapping, https://www.broadinstitute.org/connectivity-map-cmap
DAVID, https://david.ncifcrf.gov/
GenBank, https://www.ncbi.nlm.nih.gov/genbank/
GEO, https://www.ncbi.nlm.nih.gov/geo/
Human Protein Atlas, https://www.proteinatlas.org/ENSG00000136699-SMPD4/tissue/primary+data
IMPC, https://www.mousephenotype.org/data/genes/MGI:1924876
Ingenuity, https://www.qiagen.com/us/shop/analytics-software/biological-data-tools/ingenuity-pathway-analysis/#ordering information
NCBI STAR aligner tool, https://www.ncbi.nlm.nih.gov/pubmed/23104886
Neuro-MIG, https://www.neuro-mig.org/
OMIM, https://www.omim.org/

References

1. Breslow, D.K. (2013). Sphingolipid homeostasis in the endoplasmic reticulum and beyond. Cold Spring Harb. Perspect. Biol. *5*, a013326.
2. Olsen, A.S.B., and Færgeman, N.J. (2017). Sphingolipids: membrane microdomains in brain development, function and neurological diseases. Open Biol. *7*, 7.

3. Bienias, K., Fiedorowicz, A., Sadowska, A., Prokopiuk, S., and Car, H. (2016). Regulation of sphingomyelin metabolism. Pharmacol. Rep. *68*, 570–581.
4. Corcoran, C.A., He, Q., Ponnusamy, S., Ogretmen, B., Huang, Y., and Sheikh, M.S. (2008). Neutral sphingomyelinase-3 is a DNA damage and nongenotoxic stress-regulated gene that is deregulated in human malignancies. Mol. Cancer Res. *6*, 795–807.
5. Krut, O., Wiegmann, K., Kashkar, H., Yazdanpanah, B., and Krönke, M. (2006). Novel tumor necrosis factor-responsive mammalian neutral sphingomyelinase-3 is a C-tail-anchored protein. J. Biol. Chem. *281*, 13784–13793.
6. Moylan, J.S., Smith, J.D., Wolf Horrell, E.M., McLean, J.B., Deevska, G.M., Bonnell, M.R., Nikolova-Karakashian, M.N., and Reid, M.B. (2014). Neutral sphingomyelinase-3 mediates TNF-stimulated oxidant activity in skeletal muscle. Redox Biol. *2*, 910–920.
7. Dreger, M., Bengtsson, L., Schöneberg, T., Otto, H., and Hucho, F. (2001). Nuclear envelope proteomics: novel integral membrane proteins of the inner nuclear membrane. Proc. Natl. Acad. Sci. USA *98*, 11943–11948.
8. Schirmer, E.C., Florens, L., Guan, T., Yates, J.R., 3rd, and Gerace, L. (2003). Nuclear membrane proteins with potential disease links found by subtractive proteomics. Science *301*, 1380–1382.
9. Stoffel, W., Hammels, I., Jenke, B., Binczek, E., Schmidt-Soltau, I., Brodesser, S., Schauss, A., Etich, J., Heilig, J., and Zaucke, F. (2016). Neutral sphingomyelinase (SMPD3) deficiency disrupts the Golgi secretory pathway and causes growth inhibition. Cell Death Dis. *7*, e2488.
10. Sobreira, N., Schiettecatte, F., Valle, D., and Hamosh, A. (2015). GeneMatcher: a matching tool for connecting investigators with an interest in the same gene. Hum. Mutat. *36*, 928–930.
11. Vandervore, L.V., Schot, R., Kasteleijn, E., Oegema, R., Stouffs, K., Gheldof, A., Grochowska, M.M., van der Sterre, M.L.T., van Unen, L.M.A., Wilke, M., et al. (2019). Heterogeneous clinical phenotypes and cerebral malformations reflected by rotatin cellular dynamics. Brain *142*, 867–884.
12. Kircher, M., Witten, D.M., Jain, P., O'Roak, B.J., Cooper, G.M., and Shendure, J. (2014). A general framework for estimating the relative pathogenicity of human genetic variants. Nat. Genet. *46*, 310–315.
13. Huang, W., Sherman, B.T., and Lempicki, R.A. (2009). Bioinformatics enrichment tools: paths toward the comprehensive functional analysis of large gene lists. Nucleic Acids Res. *37*, 1–13.
14. Huang, W., Sherman, B.T., and Lempicki, R.A. (2009). Systematic and integrative analysis of large gene lists using DAVID bioinformatics resources. Nat. Protoc. *4*, 44–57.
15. Subramanian, A., Narayan, R., Corsello, S.M., Peck, D.D., Natoli, T.E., Lu, X., Gould, J., Davis, J.F., Tubelli, A.A., Asiedu, J.K., et al. (2017). A Next Generation Connectivity Map: L1000 Platform and the First 1,000,000 Profiles. Cell *171*, 1437–1452.e17.
16. Hetz, C. (2012). The unfolded protein response: controlling cell fate decisions under ER stress and beyond. Nat. Rev. Mol. Cell Biol. *13*, 89–102.
17. Atilla-Gokcumen, G.E., Muro, E., Relat-Goberna, J., Sasse, S., Bedigian, A., Coughlin, M.L., Garcia-Manyes, S., and Eggert, U.S. (2014). Dividing cells regulate their lipid composition and localization. Cell *156*, 428–439.
18. Smolewski, P., Grabarek, J., Halicka, H.D., and Darzynkiewicz, Z. (2002). Assay of caspase activation in situ combined with probing plasma membrane integrity to detect three distinct stages of apoptosis. J. Immunol. Methods *265*, 111–121.
19. Alcantara, D., and O'Driscoll, M. (2014). Congenital microcephaly. Am. J. Med. Genet. C. Semin. Med. Genet. *166C*, 124–139.
20. Doobin, D.J., Dantas, T.J., and Vallee, R.B. (2017). Microcephaly as a cell cycle disease. Cell Cycle *16*, 247–248.
21. Nano, M., and Basto, R. (2017). Consequences of Centrosome Dysfunction During Brain Development. Adv. Exp. Med. Biol. *1002*, 19–45.
22. Megraw, T.L., Sharkey, J.T., and Nowakowski, R.S. (2011). Cdk5rap2 exposes the centrosomal root of microcephaly syndromes. Trends Cell Biol. *21*, 470–480.
23. Morris-Rosendahl, D.J., and Kaindl, A.M. (2015). What next-generation sequencing (NGS) technology has enabled us to learn about primary autosomal recessive microcephaly (MCPH). Mol. Cell. Probes *29*, 271–281.
24. Desikan, R.S., and Barkovich, A.J. (2016). Malformations of cortical development. Ann. Neurol. *80*, 797–810.
25. Halperin, D., Kadir, R., Perez, Y., Drabkin, M., Yogev, Y., Wormser, O., Berman, E.M., Eremenko, E., Rotblat, B., Shorer, Z., et al. (2019). *SEC31A* mutation affects ER homeostasis, causing a neurological syndrome. J. Med. Genet. *56*, 139–148.
26. Braun, D.A., Rao, J., Mollet, G., Schapiro, D., Daugeron, M.C., Tan, W., Gribouval, O., Boyer, O., Revy, P., Jobst-Schwan, T., et al. (2017). Mutations in KEOPS-complex genes cause nephrotic syndrome with primary microcephaly. Nat. Genet. *49*, 1529–1538.
27. Gladwyn-Ng, I., Cordón-Barris, L., Alfano, C., Creppe, C., Couderc, T., Morelli, G., Thelen, N., America, M., Bessières, B., Encha-Razavi, F., et al. (2018). Stress-induced unfolded protein response contributes to Zika virus-associated microcephaly. Nat. Neurosci. *21*, 63–71.
28. Cho, Y.M., Jang, Y.S., Jang, Y.M., Chung, S.M., Kim, H.S., Lee, J.H., Jeong, S.W., Kim, I.K., Kim, J.J., Kim, K.S., and Kwon, O.J. (2009). Induction of unfolded protein response during neuronal induction of rat bone marrow stromal cells and mouse embryonic stem cells. Exp. Mol. Med. *41*, 440–452.
29. Laguesse, S., Creppe, C., Nedialkova, D.D., Prévot, P.P., Borgs, L., Huysseune, S., Franco, B., Duysens, G., Krusy, N., Lee, G., et al. (2015). A Dynamic Unfolded Protein Response Contributes to the Control of Cortical Neurogenesis. Dev. Cell *35*, 553–567.
30. Rutkowski, D.T., and Kaufman, R.J. (2007). That which does not kill me makes me stronger: adapting to chronic ER stress. Trends Biochem. Sci. *32*, 469–476.
31. Ryoo, H.D. (2016). Long and short (timeframe) of endoplasmic reticulum stress-induced cell death. FEBS J. *283*, 3718–3722.
32. Smith, M., and Wilkinson, S. (2017). ER homeostasis and autophagy. Essays Biochem. *61*, 625–635.
33. Orfali, N., O'Donovan, T.R., Nyhan, M.J., Britschgi, A., Tschan, M.P., Cahill, M.R., Mongan, N.P., Gudas, L.J., and McKenna, S.L. (2015). Induction of autophagy is a key component of all-trans-retinoic acid-induced differentiation in leukemia cells and a potential target for pharmacologic modulation. Exp. Hematol. *43*, 781–93.e2.

34. Rajawat, Y., Hilioti, Z., and Bossis, I. (2010). Autophagy: a target for retinoic acids. Autophagy *6*, 1224–1226.
35. Zhou, Y., Zhang, H., Zheng, B., Ye, L., Zhu, S., Johnson, N.R., Wang, Z., Wei, X., Chen, D., Cao, G., et al. (2016). Retinoic Acid Induced-Autophagic Flux Inhibits ER-Stress Dependent Apoptosis and Prevents Disruption of Blood-Spinal Cord Barrier after Spinal Cord Injury. Int. J. Biol. Sci. *12*, 87–99.
36. Bartke, N., and Hannun, Y.A. (2009). Bioactive sphingolipids: metabolism and function. J. Lipid Res. *50* (*Suppl*), S91–S96.
37. Bieberich, E. (2011). Ceramide in stem cell differentiation and embryo development: novel functions of a topological cell-signaling lipid and the concept of ceramide compartments. J. Lipids *2011*, 610306.
38. Mendelson, K., Evans, T., and Hla, T. (2014). Sphingosine 1-phosphate signalling. Development *141*, 5–9.
39. Mizugishi, K., Yamashita, T., Olivera, A., Miller, G.F., Spiegel, S., and Proia, R.L. (2005). Essential role for sphingosine kinases in neural and vascular development. Mol. Cell. Biol. *25*, 11113–11121.
40. Bamborschke, D., Pergande, M., Becker, K., Koerber, F., Dötsch, J., Vierzig, A., Weber, L.T., and Cirak, S. (2018). A novel mutation in sphingosine-1-phosphate lyase causing congenital brain malformation. Brain Dev. *40*, 480–483.
41. Suresh, S., and Osmani, S.A. (2019). Poring over chromosomes: mitotic nuclear pore complex segregation. Curr. Opin. Cell Biol. *58*, 42–49.
42. Lupu, F., Alves, A., Anderson, K., Doye, V., and Lacy, E. (2008). Nuclear pore composition regulates neural stem/progenitor cell differentiation in the mouse embryo. Dev. Cell *14*, 831–842.
43. Rasala, B.A., Orjalo, A.V., Shen, Z., Briggs, S., and Forbes, D.J. (2006). ELYS is a dual nucleoporin/kinetochore protein required for nuclear pore assembly and proper cell division. Proc. Natl. Acad. Sci. USA *103*, 17801–17806.
44. Zuccolo, M., Alves, A., Galy, V., Bolhy, S., Formstecher, E., Racine, V., Sibarita, J.B., Fukagawa, T., Shiekhattar, R., Yen, T., and Doye, V. (2007). The human Nup107-160 nuclear pore subcomplex contributes to proper kinetochore functions. EMBO J. *26*, 1853–1864.
45. Hein, M.Y., Hubner, N.C., Poser, I., Cox, J., Nagaraj, N., Toyoda, Y., Gak, I.A., Weisswange, I., Mansfeld, J., Buchholz, F., et al. (2015). A human interactome in three quantitative dimensions organized by stoichiometries and abundances. Cell *163*, 712–723.
46. Fujita, A., Tsukaguchi, H., Koshimizu, E., Nakazato, H., Itoh, K., Kuraoka, S., Komohara, Y., Shiina, M., Nakamura, S., Kitajima, M., et al. (2018). Homozygous splicing mutation in NUP133 causes Galloway-Mowat syndrome. Ann. Neurol. *84*, 814–828.
47. Rosti, R.O., Sotak, B.N., Bielas, S.L., Bhat, G., Silhavy, J.L., Aslanger, A.D., Altunoglu, U., Bilge, I., Tasdemir, M., Yzaguirrem, A.D., et al. (2017). Homozygous mutation in *NUP107* leads to microcephaly with steroid-resistant nephrotic condition similar to Galloway-Mowat syndrome. J. Med. Genet. *54*, 399–403.
48. Ungricht, R., and Kutay, U. (2017). Mechanisms and functions of nuclear envelope remodelling. Nat. Rev. Mol. Cell Biol. *18*, 229–245.
49. Kwasny, T.F. (2012). Die Rolle der nSMase3 in der Regulation des postnatalen Wachstums der Maus. PhD thesis (Cologne: University of Cologne).